Research article

Fabrication of folic acid-modified bovine serum albumin cloaked dual-drug loaded hollow mesoporous silica nanoparticles for pH-responsive and targeted delivery of gastric cancer therapy

Yuanwei Zhang [a], Yuanxiao Liang [b,*]

[a] Shengzhou Branch of Zhejiang University First Hospital, Shengzhou People's Hospital, Shengzhou, 312400, China
[b] Xinchang County People's Hospital, Xinchang, 312500, China

ARTICLE INFO

ABSTRACT

Combination therapy is a highly successful way to address the limitations of using a single treatment method and improve therapy's overall efficacy. In this study, we developed a unique hollow mesoporous silica nanoparticle (HMSN) coated with folic acid (FA)-modified bovine serum albumin (FA-BSA). This nanoparticle, referred to as HFB, was designed to target cancer cells and release dual therapeutic drugs, Indocyanine green (ICG) and Paclitaxel (PTX), in response to specific stimuli termed as HFB@IP. The BSA protein acts as a "gatekeeper" to prevent early drug releases and cargo leakage by detaching from BSA in reaction to GSH. The FA facilitates the targeted transport of the drug into cancer cells that express folate receptors (FR), enhancing the effectiveness of chemo-photodynamic treatment (PDT). The drug nanocarrier demonstrated in vitro pH/redox-triggered drug release from HFB@IP due to breaking the imine bonds between aldehyde-functionalized HMSN (CHO-HMSN) and FA-BSA with the disulfide bond inside BSA. In addition, various biological assessments, including cell uptake experiments, demonstrated that HFB@IP effectively targets SGC-7901 cells and induces apoptosis in vitro. Further, it exhibits remarkable efficiency in synergistically killing cancer cells through chemo-photodynamic therapy, as indicated by a combination index (CI) of 0.328. The results showed that combining HMSN with biodegradable stimuli-responsive BSA molecules could offer a promising approach for precise chemo-photodynamic therapy in treating gastric cancer, allowing for the controlled release of drugs as necessary.

1. Introduction

According to GLOBACAN statistics, there was an estimated 783,000 mortality and 1,033,000 new cases of gastric cancer in 2018, making it the second highest cause of cancer-related deaths globally [1]. The standard methods for treating stomach cancer include surgery, radiation therapy, and chemotherapy. In contrast, these treatments have increased survival rates, and patients' quality of life has taken a major hit due to the traumatic nature of the surgery, the inability to target the treatment, and the harmful side effects of radiation and chemotherapy [2]. The majority of gastric cancer patients are diagnosed with middle or advanced tumors (stage II or III) since the first stage presents little to no characteristic symptoms [3–5]. In many circumstances, it is still quite challenging to remove

* Corresponding author. Xinchang County People's Hospital, No. 117, Gushan East Road, Xinchang, 312500, China.
E-mail address: Yuanxiao_Liang89@outlook.com (Y. Liang).

tumors surgically [6]. Surgeons doing laparoscopic gastric cancer surgery run the risk of making inaccurate assessments of minor lesions due to a lack of haptic input. To improve the prognosis of gastric cancer patients, it is crucial to address the pressing issues of early diagnosis and exact customized intervention [7]. An alternate approach that has shown promise in recent decades is photothermal therapy, which uses heat from photothermal agents to kill tumor cells. At the same time, scientists are starting to embrace NDDS, or nanoscale drug delivery systems, which integrate imaging and treatment [8]. Not only may the administration approach that incorporates photothermal agents and nanomaterials pinpoint the exact location of the lesion, but it could also lead to more targeted, individualized treatment for the malignancy [9]. A biocompatible NDDS with tumor-targeting capability and a multifunctional theranostic drug demonstrating therapeutic and imaging activities are necessary for successful image-guided therapy [10].

Nanoparticle-based drug delivery vehicles that are triggered and targeted are seen as a suitable method to circumvent these constraints [11]. Mesoporous silica nanoparticles (MSNs) have garnered significant interest as drug carriers due to their distinct inherent characteristics, including adjustable shape, particle size, surface charges, pore size and volume, substantial specific surface area, and non-toxicity [12]. In addition, as compared to traditional MSNs, hollow MSNs (HMSNs) were discovered to have a significant drug-loading capacity because of their spacious hollow interior. This characteristic makes them more suitable as drug carriers for efficient chemotherapy [13–15]. Moreover, utilizing these nanocarriers can reduce the buildup of foreign substances in the recipient's body and mitigate the adverse impacts on healthy cells. Combinatorial chemotherapy, which involves multiple chemotherapeutic drugs, is commonly employed to enhance the therapeutic efficacy of mono-chemotherapy [16]. Furthermore, nanoparticle-based targeted and triggered drug delivery systems are also exploited. Combination chemotherapy offers advantages over mono-chemotherapy due to its ability to minimize resistance by attacking numerous therapeutic targets either sequentially or simultaneously. It also provides non-overlapping cytotoxicity and enhances the effectiveness of antitumor treatment. Combinatorial chemotherapy offers a significant benefit in its potential to produce synergistic effects [17–19].

Various theranostic agents, such as metal nanostructures, polymeric nanoparticles, carbon nanomaterials, and near-infrared (NIR) dyes, have been broadly studied for their potential in imaging-guided cancer treatment. Among these agents, indocyanine green (ICG) is the sole NIR dye that has received clinical approval [20]. Due to their transparency under NIR light, tissues provide numerous distinct advantages when using ICG. These advantages include less interference from background fluorescence, enhanced ability to penetrate deeper into tissue, and monitoring in real-time during surgical procedures [21]. Furthermore, ICG also functions as a photosensitizer, exhibiting exceptional effectiveness in converting light into heat when exposed to a specific wavelength of near-infrared light. The appealing characteristics of ICG suggest that it has the potential as a dye for tumor imaging and photothermal therapy (PTT). ICG has been employed to assess blood flow and liver function, measure cardiac output, and conduct ocular angiography [22]. However, some inherent disadvantages restrict its optimal use in clinical practice. Fluorescence quenching occurs due to the self-aggregation and instability of the solution. Furthermore, the lack of specificity towards tumors restricts its potential use in diagnosing and treating tumors. Various endeavors have addressed these difficulties, including altering ICG with ligands to enhance its targeting capability and encapsulating ICG into nanocarriers to enhance its effectiveness [23]. When comparing the former method, which typically fails to improve the stability of ICG, the latter approach (NDDS) appears to be a more promising technique for improving targeting ability, prolonging circulation, and enhancing its stability [24].

The utilization of NDDS offers numerous benefits compared to the conventional method of drug delivery. Initially, the ICG enclosed within nanoparticles can be protected from indiscriminately attaching to plasma proteins, enhancing its longevity within a living organism. Furthermore, passive targeted delivery, which relies on the enhanced permeability and retention (EPR) effects and transcytosis (perhaps including additional unidentified mechanisms), enables nanomaterials of a specified size range to traverse and remain within the tumor selectively [25]. Furthermore, the surface of nanomaterials can be altered using particular ligands to provide active targeted delivery. For example, specific receptors on the surface of cells, such as folate receptors or transferrin, are more highly expressed in tumor cells (breast and glioma cancer) [26]. Nanomaterials that have been altered with monoclonal antibodies, aptamers, and peptides can enhance the process of cellular uptake through receptor-mediated endocytosis (RME). Integrins are a group of receptors located in the cell membrane that may transmit signals in both directions across the membrane [27]. These signals are involved in processes such as invasion, migration, survival, and proliferation. Paclitaxel (PTX) is a widely used chemotherapeutic drug for treating several types of cancer, such as lung and breast cancer. Nevertheless, the absorption of PTX in tumor cells is diminished due to the efflux mediated by P-glycoprotein (P-gp) [28]. Nanoparticles (NP) are an optimal means of delivering drugs to the brain by traversing biological barriers. Encapsulating drugs within NPs effectively improves the bioavailability of target-specific delivery and reduces the harmful effects of therapeutic drugs [29]. PLGA, an FDA-approved polymer, is widely used to encapsulate and deliver hydrophobic pharmaceuticals like PTX [30]. It facilitates the efficient ingestion of the drug into tumor cells by mechanisms like phagocytosis or endocytosis. Their biodegradability and biocompatibility are exceptional.

Various "gatekeepers" have been developed for keeping drugs and "intelligently" releasing cargo by eliminating clogged portions in reaction to physical and drug stimuli, allowing for drug release "on-demand" in an exact milieu [31]. The unequal distribution of glutathione (GSH) between the blood levels (2–20 μM) and the cellular cytoplasm (2–10 mM) makes it an attractive induction between the series of regulated drug releases. Redox-triggered drug delivery carried by vehicles utilizing disulfide bonds is believed to accomplish the "on-demand" drug release, drawing inspiration from the fact that they are biodegradable by the GSH and naturally occurring in extracellular vessels [32].

Bovine serum albumin (BSA), a safe macromolecule, has been extensively used in biochemical and medical research due to its non-toxic, on-antigenic, and excellent biocompatibility properties [33]. Significantly, intramolecular disulfide bonds and abundant functional groups bind BSA molecules cloaked with other substances to develop innovative drug nanocarriers for redox reactions without the need for the complicated pyridyl disulfide exchange reaction [34]. Multiple stimuli response approaches have been applied to cancer tissues to improve the exact drug's release ability. Cancer tissues have lower extracellular (pH ≈ 6.8) pH values than

normal tissues and the bloodstream. Furthermore, lysosomes and endosomes inside cells display lower (<5.4) pH values. Based on the dynamic imine relation, it is extensively demoralized to develop pH-switchable nanocarriers [35]. Additionally, folic acid (FA), a commonly used targeting ligand, was embedded in the surface of BSA. This modification enables the successful targeting of tumor cells and the precise delivery of drug therapies specifically to the tumor cells. Consequently, this would result in a notable enhancement in cancer treatment and a reduction in the adverse impacts on healthy cells or tissues [36–38].

Therefore, HFB@IP, a targeted nanoplatform of HMSNs (drug nanocarrier) and BSA (gatekeeper), was fabricated to respond to pH and redox. Imine bonds were used to link BSA to HMSNs, and the nanoparticles' enhanced biostability and compatibility stopped the drug from leaking and allowed for pH/redox dual-response release. The release of drugs from the nanocarrier and induction of cell apoptosis was caused by the gradual degradation of the nanoparticles' shell into fragments, eventually breaking. This degradation was triggered by high glutathione concentration and intracellular acidity. The released ICG molecules under irradiation (635 nm) successfully produced reactive oxygen species (ROS), a cytotoxic drug that further causes harm to target tissues and enhances treatment efficacy. Investigation at nanocarriers affected the induction of death of SGC-7901 cancer cells in vitro to study the potential uses of vectors. The developed nanocarrier is anticipated to enhance the targeted drug delivery system and improve combination in gastric cancer treatment.

2. Experimental section

2.1. Material and reagents

Tetraethylorthosilicate (TEOS), hydrochloric acid (HCl), cetyltrimethylammonium bromide (CTAB), sodium carbonate (Na_2CO_3), ammonia solution, ethanol, and methanol were acquired from Dalian MeiLun Biotechnology Co., Ltd. Triethoxsilylbutyraldehyde (TESBA) and Tris (hydroxymethyl) methyl aminomethane (APTES) were obtained from Bloomage Freda Biopharm Co., Ltd. Indocyanine green (ICG), Paclitaxel (PTX) and Bovine Serum Albumin (BSA) were purchased from Shanghai Titan Science Co. (Shanghai, China). Folic acid (FA) and 1,3-Diphenylisobenzofuran (DPBF) were bought from Fuzhou Feixing Biotechnology Co., Ltd. NHS and EDC·HCl were acquired from Hongquan Biotechnology Co., Ltd. Live/Dead cell imaging kits, DAPI, and annexin V-FITC and propidium iodide (PI) were purchased from Thermo Fisher Scientific (Waltham, MA, USA). Gibco provided fetal bovine serum (FBS), Dulbecco's modified Eagle's medium (DMEM), Tyrisin, and L-glutamine. 3-(4,5-di-methylthiazol-2-yl)-2,5-diphenyl tetrazolium bromide (MTT) was bought from Dojindo Laboratories (Kumamoto, Japan). All other chemicals were available from commercial sources and used without further purification.

2.2. Characterization

The morphologies of obtained nanoparticles were investigated by TEM (transmission electron microscopy), characterized by a JEOL JEM-1011 electron microscope operating at an acceleration voltage of 100 kV. Zetasizer Nano ZS90 instrument (Malvern, Westborough, MA) was employed to collect these samples' zeta potential and hydrodynamic size distribution. CLSM (confocal laser scanning microscopy) images were taken using a Zeiss LSM 700 (Zurich, Switzerland). UV–Vis absorption spectra of obtained target products were tested with a Shimadzu UV-2450 PC UV/Vis spectrophotometer. FT-IR spectra of as-prepared NPs were monitored on a Nicolet Impact 410 spectrometer. Thermogravimetric analysis of obtained NPs was recorded utilizing a NetzchSta 449c thermal analyzer system at a 10 °C/min rate under an air atmosphere. Fluorescence images of cells were obtained using a fluorescence microscope (Olympus IX71), and the fluorescence intensity was measured using ImageJ software (https://imagej.net/ij/).

2.3. Preparation of HMSNs-CHO

The SiO_2 nanoparticles were developed using the Stober technique [39]. TEOS (5 mL) was immersed in a combination solution of ethanol/water/ammonia solution (107 mL/15 mL/2.5 mL) and stirred vigorously at 30 °C for 2 h to acquire solid silica nanoparticles ($sSiO_2$). Next, additional fabrication of SiO_2@CTAB-SiO_2 nanoparticles was performed. CTAB (0.25 g) was immersed in a mixed solution of water/ethanol/ammonia solution (45 mL/45 mL/0.9 mL), and then 30 mL of SiO_2 solution was added evenly. Following 30 min of stirring, 0.4 mL of TEOS was promptly introduced, and the reaction was maintained for 6 h. After centrifugation, the outcome was uniformly distributed in an 80 mL aqueous solution. Subsequently, 2 g of sodium carbonate (Na_2CO_3) were introduced and allowed to react at 50 °C for 20 h to corrode the SiO_2 core. The precipitates were obtained through centrifugation and rinsed thrice with ethanol and deionized water, respectively. Ultimately, the raw product was dispersed and suspended using ultrasonic waves into a combination of methanol and hydrochloric acid (50 mL/3 mL). The resulting mixtures were then heated at 80 °C for 48 h. HMSNs were obtained by collecting the precipitate through centrifugation and washing it six times with methanol and distilled water.

Aldehyde-functionalized hollow mesoporous silica nanoparticles (HMSNs-CHO) were fabricated using the approach described in the published literature. In the usual procedure, HMSNs (150 mg) were heated at 80 °C with TESBA (300 μL) and anhydrous toluene (30 mL) for 20 h in a nitrogen environment. The HMSNs-CHO products were obtained using centrifugation and subjected to three rounds of washing with methanol and acetone, respectively. Subsequently, the HMSNs-CHO nanoparticles underwent a vacuum drying process at 50 °C for 12 h.

2.4. Preparation of BSA-FA

The carboxylic groups of the FA were conjugated with the amino groups of the BSA through the amide reaction. The detailed fabrication process is as follows: FA (40 mg, 0.09 mmol) immersed in DMSO was reacted with EDC·HCl (32.48 mg, 0.18 mmol), NHS (20.86 mg, 0.18 mmol), and 200 μL TEA by stirring in the dark for 2 h to form an active ester intermediate (NHS-folate). Then, the pre-activated FA-NHS was mixed dropwise with the 200 mg BSA. The reaction mixture was kept at 35 °C for 24 h. The obtained mixed solution was dialyzed for four days with PBS (0.1 M, pH = 7.4) and deionized water via a dialysis bag (MWCO 8000 Da) to remove the byproducts and excess reactants. The FA-BSA obtained eventually were yellow powders after dialysis and lyophilization. The molar ratio of FA and BSA was 1:30.

2.5. Drug loading and fabrication of HFB@IP NPs

The specific fabrication methods of HFB (CHO-HMSNs-BSA-FA) and drug loading BSA-FA [40]. The outlets of HMSNs were capped with BSA-FA through reversible imine linkage between the aldehyde group of HMSNs-CHO and the amine group of BSA at pH = 8.0. Herein, HMSNs-CHO (50 mg) dispersed in a 25 mL PBS solution was mixed with PTX (3 mg/mL) and ICG (2 mg/mL), stirring for 24 h. Subsequently, BSA-FA (50 mg) was dispersed into 25 mL PBS solution and added to the above solution, stirring for 24 h. The products were obtained by centrifugation and washed extensively to remove the unabsorbed drug and unmodified BSA-FA. The amount of the loaded drug was evaluated through UV–vis absorption at 480.5 nm and 664.5 nm by subtracting the amount of the unloaded PTX and ICG in the obtained supernatant from the amount of the original feeding drug. The drug loading efficiency (DL) and drug entrapment efficiency (EE) were estimated as follows:

DL (%) = Mass of loaded drug/Mass of drug-loaded HFB@IP × 100 %
EE (%) = Mass of loaded drug/Total dosage × 100 %

2.6. Assessment of PDT performance

The 1,3-Diphenylisobenzofuran (DPBF) was used as a probe to measure the levels of reactive oxygen species (ROS) by measuring the absorption at 418 nm. 2 mL solution of 7 μg/mL of DPBF in DMSO was combined with 4 mL suspensions of 100 μg/mL of HFB@IP. Next, the solution mixtures were exposed to a 636 nm laser with an intensity of 100 mW/cm^2 for varying durations of 0, 10, 20, 60, 120, and 150 s. The UV–vis spectroscopy was used to evaluate the absorption strength at a wavelength of 417 nm. The groups of nanoparticles without ICG were utilized as control samples [41].

2.7. Evaluation of pH/GSH-triggered drug release

The in vitro drug release profile of HFB@IP was investigated in various buffer solutions of pH = 5.0, 6.0 and 7.4, 5.0, pH = 5.0 + 10 mM (GSH), and pH = 7.4 + 10 μM (GSH) HFB@IP were dispersed in 1 mL of the corresponding buffer solution to the final concentration of 5 mg/mL, and then the solutions were sealed in a dialysis bag with an MWCO of 14 kDa. The dialysis bag was immersed in 10 mL buffer solutions of pH = 7.4, pH = 6.0, pH = 5.0, pH = 7.4 + 10 μM GSH, and 5.0 + 10 mM GSH. Of HFB@IP and placed in a shaker at 37 °C. Within a specified time interval, 1 mL sample solution was removed from the buffer solution, and an equivalent amount of fresh buffer solution was added. Meanwhile, the concentration of ICG/BCNU in the solutions at different time points was determined by UV–vis [42].

2.8. Examination of nanoparticle stability

HMSNs and HFB (20 mg) stability were evaluated in 5 mL of PBS (pH = 7.4). At various days (0–3). Dispersibility was monitored by observing the Zeta potential and particle sizes investigation of the HMSNs and HFB, which Nano ZS90 Zetasizer monitored.

2.9. Cell culture

Human gastric carcinoma (SGC-7901 and MGC80-3), and human gastric epithelial cells (NCI-N87) cells were cultured at 37 °C under 5 % CO$_2$ in the air with regular growth medium high-glucose DMEM with 10 % FBS, 1 % penicillin/streptomycin. The Chinese Academy of Sciences (Shanghai, China) purchased all the cancer cell lines.

2.10. In vitro cell uptake

In brief, SGC-7901 and NCI-N87 cells were planted and cultured separately at 37 °C for 24 h. Next, the DMEM medium was removed, and different samples dispersed in a fresh medium were mixed and incubated for 4 h to detect cellular uptake (Dil labeled PTX concentration: 5 μg/mL). Then, the nuclei were stained by a blue probe (DAPI) for 10 min. Lastly, the cells were rinsed several times with PBS and checked using CLSM. Free FA (FA concentration: 100 μg/mL) was incubated with SGC-7901 and NCI-N87 cells for 4 h to explore its competitive inhibition on the endocytosis of different nanoparticles. The sample groups were PTX, ICG + PTX, HFB@IP, and HFB@IP with free FA [43].

2.11. Assessment of cytotoxicity

The MTT assay was used to investigate the cytotoxicity of the HFB@IP in SGC-7901 cells and MGC80-3 cells. SGC-7901 cells and MGC80-3 cells were first seeded in 96-well plates at a density of 2×10^3 cells per well. After 24 h incubation, the original medium was removed, followed by treatment with fresh culture medium containing ICG, PTX, HFB@IP, and HFB@IP + Laser at different concentrations for 24 h. The medium was discarded, the cells were washed several times with PBS, and MTT (0.5 mg/mL, 100 μL) was added to each well and incubated for 4 h at 37 °C. Subsequently, 150 μL of DMSO was dispensed to each well. After shaking for 10 min, the absorbance of each well at 490 nm was measured with a microplate reader [44].

The ICG, ICG@HFB, and HFB@IP were co-incubated with SGC-7901 and MGC80-3 cells to investigate the synergic therapeutic result of chemo-photodynamic treatments. After 2 h, the cells were irradiated (100 mW/cm^2) for 10 min by a 635 nm laser. As reported previously, the biocompatibility of ICG, ICG@HFB, and HFB@IP with blood samples was assessed through a hemolysis assay. Briefly, 10 mL samples of blood were collected from healthy rabbits via the ear vein, and fibrinogen was removed by vigorously stirring these samples using a glass rod. After adding 5 mL of saline, samples were centrifuged thrice until the supernatants were transparent. Then, 2 mL of the prepared red blood cell precipitates were combined with 98 mL of saline solution to yield a 2 % red blood cell suspension. This suspension (2.5 mL) was then mixed with different ICG, ICG@HFB, and HFB@IP concentrations (12.5–100 μg/mL) in four separate tubes (1–4), with saline (Tube 5) and deionized water (Tube 6) respectively serving as negative and positive controls [45]. Following a 4 h incubation at 37 °C, these red blood cell suspensions were examined for hemolysis. We calculated the combination index (CI) chemo-photodynamic therapy. The CI value can then be calculated by fitting the logarithmically transformed data to a linear reversion equation that includes the sigmoiditis of the curves, the growth inhibitory factor of each drug, and IC$_{50}$. The CI value might be = 1 (additive), >1 (antagonistic), or <1 (synergistic effect) of the drug combination.

2.12. Intercellular imaging studies

For intracellular observation of singlet oxygen detection, 8×10^4 cells were planted onto plastic-bottomed μ-dishes (35 mm) with culture medium and incubated for 24 h. The medium was removed, and cells were rinsed thrice with PBS (pH = 7.4). Then, Dil = 5 μg/mL in fresh DMEM medium was added to each well, and the plate was incubated for 4 h at 37 °C. Later, dichloro-dihydro-fluorescein diacetate (DCFH-DA, 100 M) was mixed and incubated for 1 h at 37 °C, and the cells were irradiated (100 mW/cm^2) by a 635 nm laser for 10 min. Then, the cells were rinsed thrice with PBS (pH = 7.4) and fixed with 4.0 % formaldehyde (1 mL) at 35 °C for 15 min. After ringing with PBS (pH = 7.4), the cells were subjected to confocal microscopy and flow cytometry observation.

For subcellular distribution observation, 8×10^4 SGC-7901 cells were seeded onto plastic-bottomed Ibidi μ-dishes (35 mm). After being washed three times with PBS (pH = 7.4), the cells were incubated with NAC, Z-VAD-FMK, and Nec-1 in a culture medium at 37 °C for 12 h. After incubation, the cells were washed thrice with PBS (pH = 7.4) at room temperature for 15 min. The ICG and HFB@IP groups were then subjected to a 635 nm laser. Cell counting CCK-8 was used to examine the cell viability.
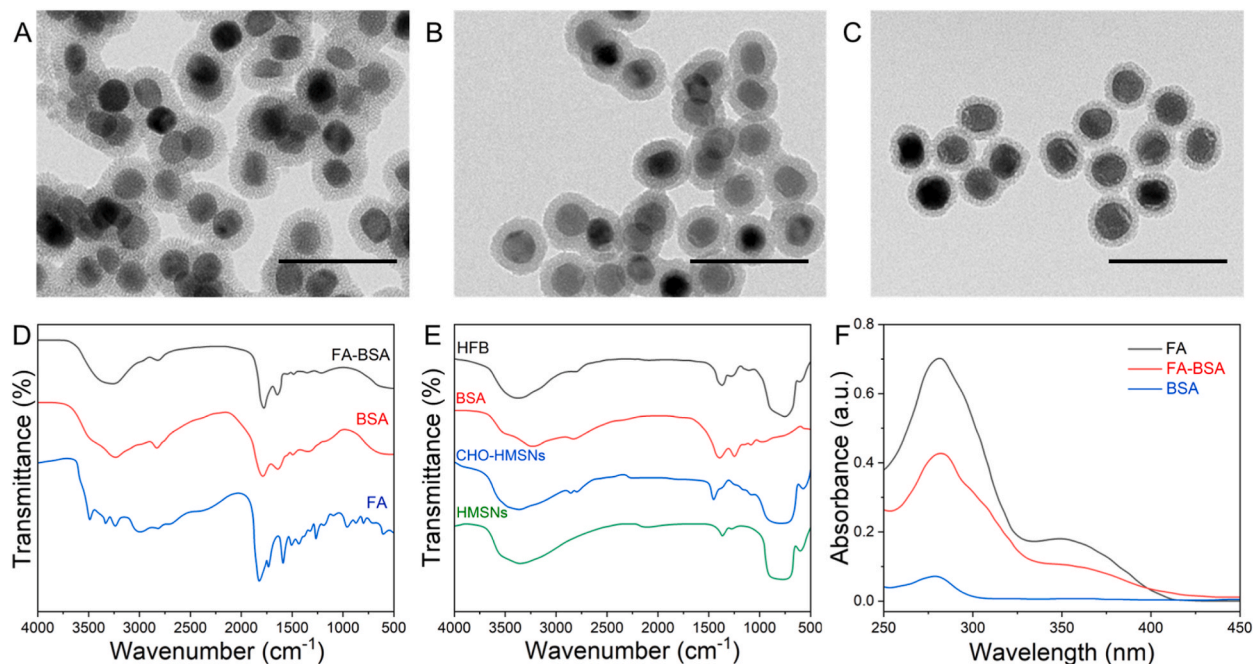

Fig. 1. Transmission electron microscope (TEM) images of (A) HMSNs, (B) HFB, and (C) HFB@IP. Scale bar 100 nm. (D) and (E) Fourier-transform infrared (FT-IR) spectral images of various formulations. (F) Ultraviolet–visible spectral (UV–Vis) absorption spectral images of BSA, FA, FA-BSA.

Acridine orange and ethidium bromide (AO/EB) staining of apoptosis cell morphology. First, 8×10^4 SGC-7901 and MGC80-3 cells were seeded onto plastic-bottomed μ-dishes (35 mm) with culture medium and incubated for 24 h. Then, the medium was changed with a fresh medium containing IC_{50} concentration of ICG, PTX, HFB@IP, and HFB@IP + Laser at 37 °C for 12 h. Finally, the cells were incubated with AO/EB staining (5 mg/mL, 30 min, 37 °C) and detected by fluorescence microscopy [46].

Annexin V-FITC/PI staining was used to assess the apoptosis mode of cell death. First, 8×10^4 SGC-7901 and MGC80-3 cells were planted on a 6-well plate with culture medium and incubated for 24 h. Then, the medium was replaced with a fresh medium containing an IC_{50} concentration of ICG, PTX, HFB@IP, and HFB@IP + Laser at 37 °C for 24 h. The cells were collected and resuspended in 100 μL of cold binding buffer, followed by adding 5 μL of Annexin V-FITC and 5 μL of PI solution. Data were collected based on the counting of 20,000 events. Each sample was tested 3 times. The cells treated with PBS were used as control. Then, the fluorescence of cells was analyzed using a FACSCanto II cytometer (BD Biosciences) [47].

2.13. Statistical analysis

All measurements were performed in triplicate, and the mean value and standard deviation (mean $\pm$ SD). The statistical analysis of different groups was compared through Student's t-test (*$p < 0.05$ was considered statistically significant. **$p < 0.01$ and ***$p < 0.001$ were considered highly significant).

3. Results and discussion

3.1. Characterization of BSA-FA and nanoparticles

To develop the FA-BSA molecule, which regulated the encapsulation and on-demand release of drugs and performed HMSNs for cancer cell targeting, FA was covalently bonded to the BSA protein via an amidation (Fig. 1D). The FA-BSA fabrication was characterized using FTIR spectroscopy and UV–Vis. Fig. 1E shows that when comparing the individual BSA and FA molecules, the band at 921 cm^{-1} that belonged to γ(-OH) in FA vanished, while the peak at 605 cm^{-1} for lysine in BSA emerged. The broad N-H and O-H stretching vibration in BSA-FA is considered to be responsible for the broad peak at about 3510 cm^{-1}. In addition, the amino bond of FA-BSA conjugates was indicated by the additional peaks at 1545 cm^{-1} for N-H and 1650 cm^{-1} for C-O. Fig. 1F further shows that while raw BSA only has a single absorption peak at 279 nm, FA has two distinct bands at 282 and 348 nm. The effective fabrication of FA-BSA was confirmed by its absorbance at 346 nm.

By the interaction of aldehyde-terminated silane with the HMSNs surface silicon hydroxyl group, the aldehyde-functionalized HMSNs (CHO-HMSNs) developed. While the folic acid modification acts as a targeted ligand, BSA-FA binds to the CHO-HMSNs to
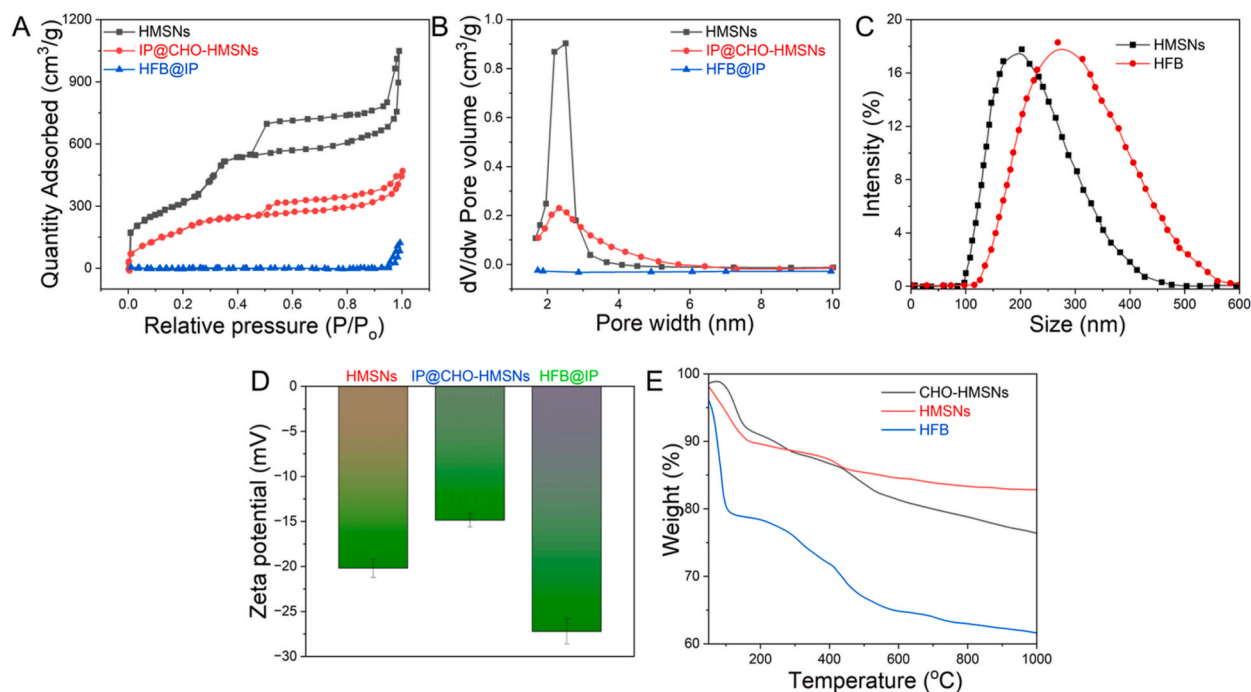

Fig. 2. (A) N2 Adsorption and Desorption (Brunauer-Emmett-Teller, BET) of HMSNs, IP@CHO-HMSNs, and HFB@IP. (B) BJH pore volume distributions of HMSNs, IP@CHO-HMSNs, and HFB@IP. (C) Hydrodynamic size distribution of HMSNs and HFB. (D) Zeta potential of HMSNs, IP@CHO-HMSNs, and HFB@IP. (E) Thermogravimetric analysis (TGA) curves of HMSNs, CHO-HMSNs, and HFB.

attain "gatekeeper" effects after pore loading with PTX and ICG. With a low polydisperse index (PDI, 0.185), the average hydrodynamic diameter of HMSNs was 209 ± 8 nm, as demonstrated in Fig. 2C. The observed increase in particle size to 241.4 ± 6 nm in the modified nanoparticles (HFB) compared to the naked HMSNs indicates that BSA-FA was transformed. In Fig. 1A–C, the transmission electron microscopy (TEM) image revealed that HMSNs had a consistent spherical shape (mean size of 139.4 ± 7 nm) and a distinct hollow mesoporous morphology. Fig. 2C showed that the surface immobilization of BSA-FA was evident, as the outer coating of HFB became blurry and the shell size increased by 16 ± 2 nm.

The characteristic BET curves to Type 4 isotherms demonstrate that HMSNs have a well-defined, homogeneous, and ordered mesoporous structure (Fig. 2A). Because of the BSA-FA molecule coating, the diffraction peak vanished in HFB, and the surface area ($2.54 \text{ m}^2/\text{g}$) dropped dramatically when related to the HMSNs ($1015 \text{ m}^2/\text{g}$) (Fig. 2B). The successful capping of BSA-FA was confirmed by the corresponding tendency in the nanoparticles' pore width and volume, as shown in Fig. 2B. The HMSNs changed from -20.9 ± 2.31 mV to -16.21 ± 3.1 mV when related to HMSNs-CHO; the reduction of hydroxyl groups caused this change (Fig. 2D). In addition, the effective modification of the BSA-FA was further confirmed when the charge of HFB became -26.8 ± 3.3 mV, resulting from the negatively charged carboxyl group of the BSA molecule and folic acid (isoelectric point 4.8). Similarly, the BSA-FA alteration was confirmed by the variation in zeta potential and weight reduction in TGA, as illustrated in Fig. 2E. The TGA diagram showed that reducing cloaked BSA-FA on HMSNs was responsible for 39.12 % of the additional weight loss in HFB compared to HMSNs (17.97 %). Lastly, the successful alteration of the BSA and aldehyde groups is indicated by characteristic C-double bond stretching vibrations at 1725 cm^{-1} and the amide (NH_2) bonds of the carboxyl group at 1651 and 1550 cm^{-1} (Fig. 1E).

The stability of nanoparticles assesses the therapeutic use of drugs in the physiological milieu [48]. BSA enhanced the physiological stability of HMSNs and served as a gatekeeper to accomplish stimuli-responsive drug release in our work. HFB exhibited excellent stability following 12 h of incubation in PBS (pH = 7.4). Fig. 3A shows that during 15 days, the hydrodynamic size of HFB was 228–248 nm with a low PDI of less than 0.3. Also, as shown in Fig. 3B, there was a little shift in the zeta potential across all samples. These findings suggest that HFB has excellent colloidal stability, which would increase the delivery systems.

3.2. Drug loading and in vitro release behaviors

PTX and ICG were loaded onto the resulting HMSNs-CHO nanoparticles before adding BSA-FA, which formed dynamic imine bonds to encase the mesoporous carriers. Centrifugation and washing were the last steps in obtaining BSA-FA-gated nanoparticles (HFB@IP). 39.31 % of the total PTX and 27.37 % of the total ICG were loaded.

The extracellular pH values of tumor tissues are typically lower (pH = 6.5–6.8) than those of normal tissues and circulation (pH = 7.3). The pH values of endosomes and lysosomes within cells are significantly lower, often reaching pH = 5.5 and 4.5, respectively. To
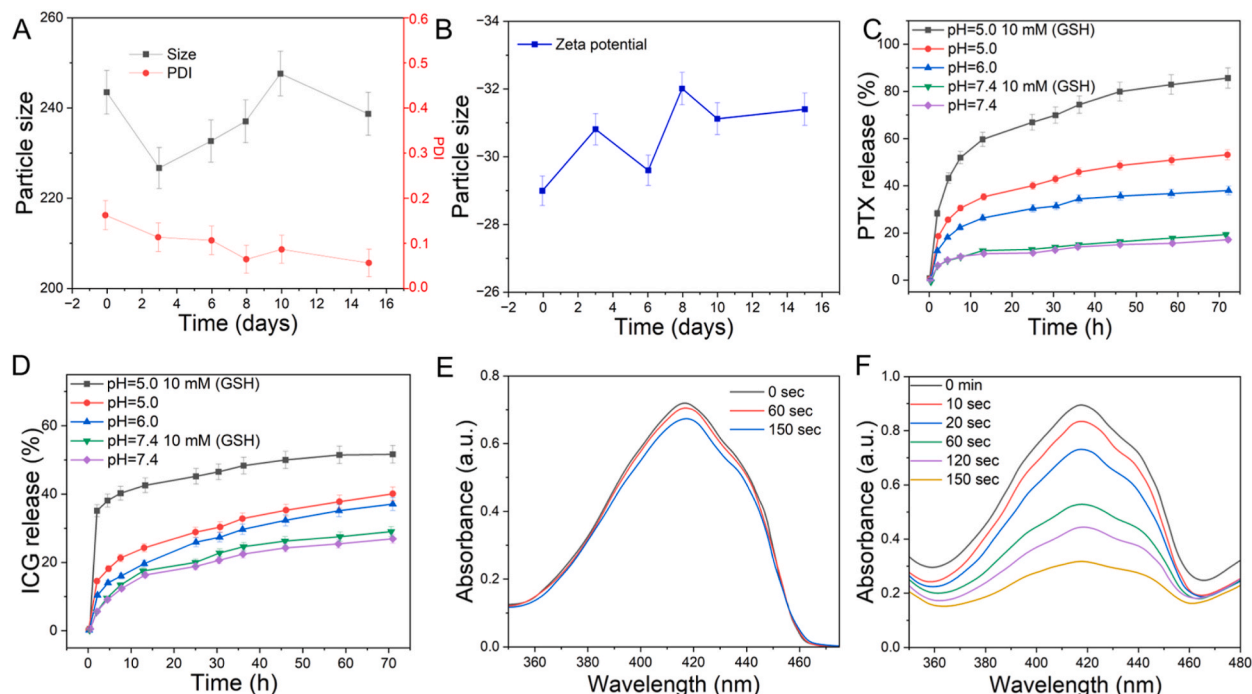

Fig. 3. (A) The variations in the hydrodynamic size of HFB@IP with 15 days incubation. (B) Zeta potential of HFB@IP with 15 days incubation. (C) In vitro PTX release from HFB@IP. (D) In vitro ICG release from HFB@IP. (E) UV–Vis spectral analysis of HFB@IP after laser irradiation 635 nm with (100 mW/cm^2). (F) Fluorescence analysis of HFB@IP after laser irradiation 635 nm with (100 mW/cm^2) by DPBF (fluorescent probe). The data are represented as mean $\pm$ standard deviation (SD).

assess the pH-responsive drug release characteristics of HFB@IP, we used buffers with varying pH values (pH = 7.4, 6.0, and 5.0) as solvents, simulating the milieu during drug delivery. Fig. 3C shows that at pH = 7.4, PTX had an admirable gating action under the physiological milieu, with a release of less than 13 % over 72 h. At acidic pH = 6.0 and 5.0, the PTX release rate was 30.4 % and 53.5 %, a considerable increase. The detachment of the gatekeeper (BSA-FA) via cleaving the imine bonds among BSA and HMSNs-CHO is likely responsible for the pH-dependent drug release. Similarly, ICG release was more remarkable at a pH of 5.0 compared to 7.0. Stable BSA-FA capping may limit drug leakage under the physiological milieu (pH = 7.4), according to the pH-dependent drug release behaviors. The drug's release rate accelerates when BSA-FA detaches from its imine linkages in an acidic milieu.

To study the GSH-responsive drug release behavior of HFB@IP in a model of the extracellular milieu, we placed it in a buffer with a pH = 7.4 and added 10 μM of GSH. We then placed it in a buffer with a pH = 5.0, which mimics the intracellular milieu. The cumulative drug release of PTX was 19.1 % under the physiological milieu, supporting the stability of the nanoparticles, even with a low quantity of GSH (10 μM). It is worth mentioning that when subjected to 10 mM GSH (pH = 5.0), the PTX release increased dramatically to 85.3 % and the ICG release to 51.5 %, respectively (Fig. 3D). Possible explanations for this phenomenon include: First, the disulfide bonds in the BSA molecule are broken when the concentration of GSH is high, which breaks the BSA into smaller pieces and speeds up the drug release. Second, when exposed to an acidic buffer, the acid-sensitive imine bonds among the HMSNs-CHO and BSA are more accessible to disruption, which speeds up the drug release even more. Third, because PTX is protonated, its solubility increases in an acidic milieu (pKa of 8.3), and PTX diffuses faster than ICG in an acidic milieu.

3.3. In vitro PDT performance of HFB@IP

By measuring the variation in absorbance of DPBF at 418 nm following 635 nm laser irradiation (100 mW/cm^2), the PDT performance of different NPs may be investigated by DPBF as a ROS probe. Fig. 3E indicates that when bare carrier HFB was exposed to NIR radiation 635 nm, the UV absorption curves of DPBF hardly changed. The HFB@IP shows a notable drop in absorbance at 417 nm because $_1O^2$ produced by photosensitizer ICG oxidized DPBF (Fig. 3F). These findings demonstrate the photodynamic therapeutic
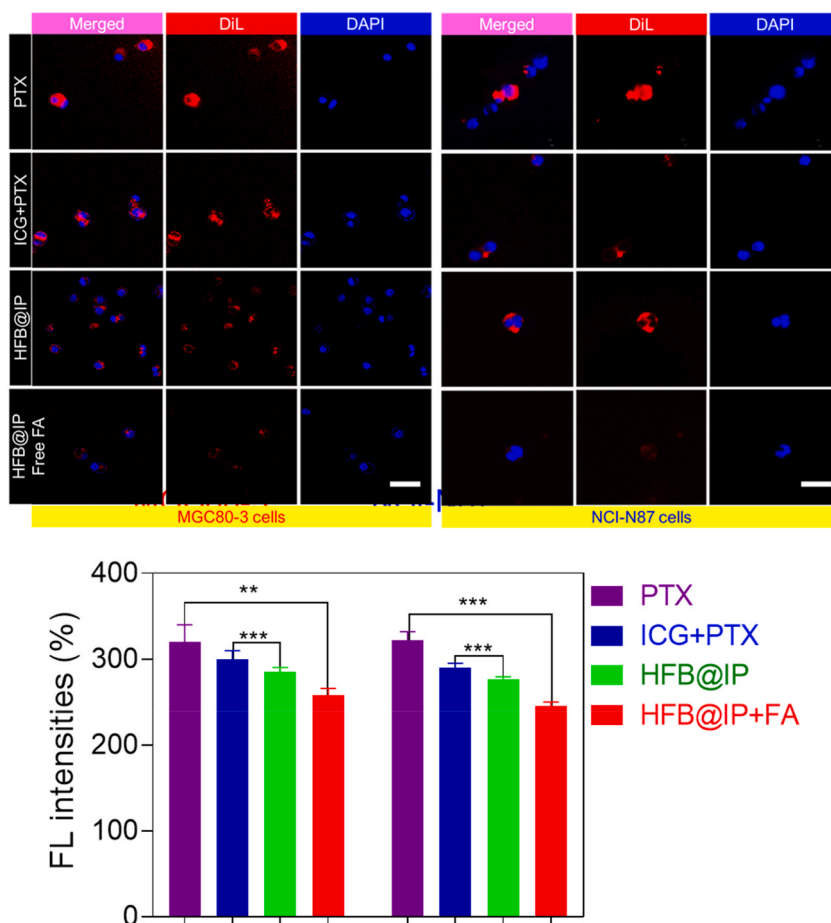

Fig. 4. Confocal Laser Scanning Microscopy (CLSM) images of MGC80-3 and NCI-N87 cells after incubation with DiL labeled PTX, ICG + PTX, HFB@IP, and HFB@IP + free FA. Scale bar 40 μm. The bar diagram indicates ImageJ analysis of the cellular uptake fluorescence intensities of ICG, PTX@HFB, HFB@IP, and HFB@IP + FA. The data are represented as mean ± standard deviation (SD). (*$P < 0.05$, **$P < 0.001$, and ***$P < 0.01$).

potential of synthetic nanoparticles by showing their ability to produce reactive oxygen species.

3.4. In vitro cellular uptake and cytotoxicity

Nanoparticle uptake efficiency in MGC80-3 and NCI-N87 cells was assessed in confocal microscopy fluorescence imaging (CLSM) assays [49]. Free PTX could enter cells via free diffusion without remarkable selectivity, as shown by the significant fluorescence intensities in both types of cells (Fig. 4). Adverse effects on normal cells due to such nonspecific cellular uptake would be severe and poisonous. Compared to NCI-N87 cells, MGC80-3 cells exhibited a substantially greater DiL labeled-PTX fluorescence signal from HFB@IP. Folate modification may enhance the targeted cellular absorption of nanoparticles in MGC80-3 cells overexpressing the folate receptor, according to the varied cellular uptake efficacy. The folate receptor-mediated route was blocked by pre-incubating the MGC80-3 cells with free FA to provide more evidence of FA-dependent improved cellular internalization. The cellular uptake of nontreated control, laser alone, free HFB, HFB@IP with and without laser of NCI-N87 cells, and MGC80-3 cells were shown in Fig. S1. As predicted, the targeting capability of FA-decorated HFB@IP was confirmed when free FA dramatically reduced the red fluorescence in cells treated with HFB@IP.

SGC-7901 cells, MGC80-3 cells, and NCI-N87 cells were utilized in the MTT experiment to examine the cytotoxicity of various samples. SGC-7901 and MGC80-3 cells were treated with different samples to determine the in vitro anticancer effect. First, in the group that had photodynamic therapy (ICG and ICG + Laser, ICG@HFB + Laser), the group that received free ICG + Laser demonstrated increased cytotoxicity compared to the group that did not get laser treatment. This indicates that photosensitizer ICG can cause cell damage and hinder the survival of SGC-7901 cells when exposed to laser light. The cytotoxicity to SGC-7901 cells was much higher with ICG@HFB + Laser than with ICG + Laser, probably because the cellular uptake improved. Next, Fig. 5A shows the SGC-7901 cell cytotoxicity as a function of dose for both free PTX and PTX@HFB at concentrations from 0.0625 to 4 μg/mL. Even at the same dose of PTX, the toxicity of PTX@HFB was much higher than that of free PTX. PTX@HFB was more harmful than free PTX because the nanoparticles were taken up by cells more efficiently through FA-receptor-mediated endocytosis. A noteworthy finding was that SGC-7901 cell viability was significantly reduced following HFB@IP + Laser treatment compared to PTX and ICG + Laser. This suggests that chemo-photodynamic therapy can inhibit cancer cells effectively at low concentrations.

Similar cell cytotoxicity was detected in MGC80-3 cells treated with various samples. Fig. 5B shows that in contrast to free PTX and ICG + Laser, the HFB@IP + Laser could significantly suppress MGC80-3 cell growth even at deficient PTX concentrations (0.25–1 μg/mL). The results show that the nanoparticles modified with FA can be highly targeted to MGC80-3 cells and that HFB@IP NPs can combine chemotherapy and PDT to generate impressive apoptosis. In addition, the IC_{50} concentrations of PTX, HFB@IP, and HFB@IP + Laser in SGC-7901 cells for 4.02, 44.57, 2.87, and 1.68 μg/mL, respectively. IC_{50} of PTX, HFB@IP, and HFB@IP + Laser in MGC80-3 cells for 0.52, 11.24, 0.64, and 0.12 μg/mL, respectively. Importantly, in MGC80-3 cells, the IC_{50} ratio of HFB@IP + Laser was 0.12 μg/
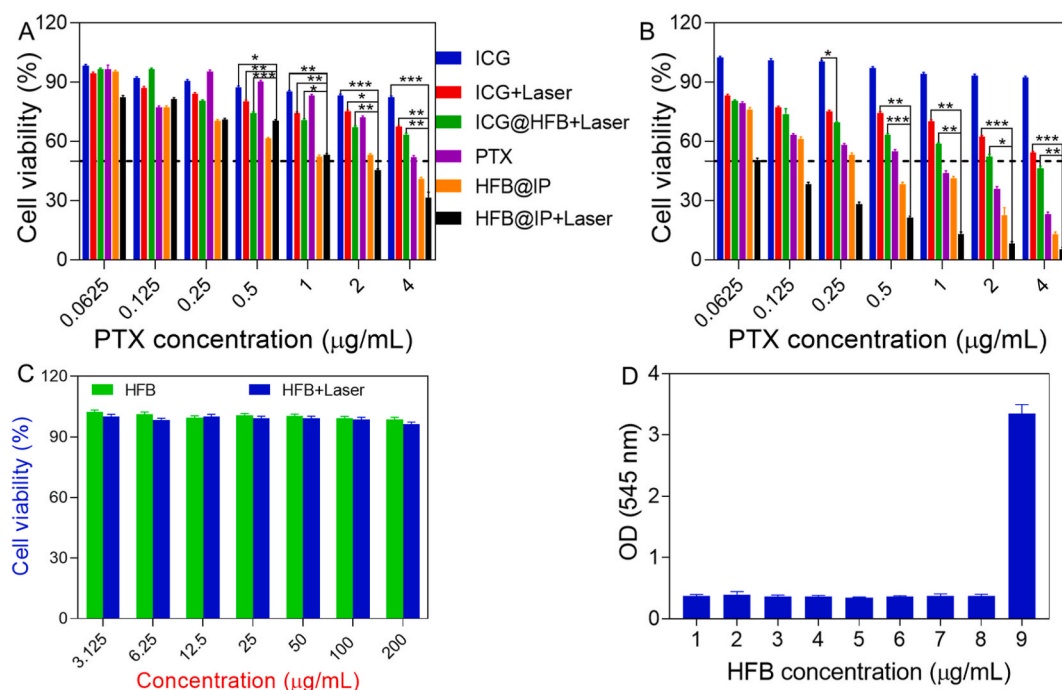

Fig. 5. In vitro cell viabilities of (A) SGC-7901 and (B) MGC80-3 cells incubated with ICG, ICG + Laser, ICG@HFB + Laser, PTX, HFB@IP, HFB@IP + Laser. (C) In vitro relative viabilities of NCI-N87 cells incubated with HFB in the dark and laser for 10 min. D) Hemolysis assay of HFB. The data are represented as mean ± standard deviation (SD). (*$P < 0.05$, **$P < 0.001$, and ***$P < 0.01$).

mL, approximately thirteen times lower than the free PTX concentration of 0.52 μg/mL. This suggests that the HFB@IP NP nanoparticles can block cell activity and enhance cell death to the highest degree. The results of the combination index (CI) analysis show that the chemotherapy and photodynamic therapy of HFB@IP NPs had a synergistic impact, with a value of 0.326 for the Free PTX and HFB@IP + Laser group and a value of 0.086 for the ICG + Laser and HFB@IP + Laser group. Finally, chemo-photodynamic combination therapy, which combines HFB@IP with laser irradiation, is more effective than monotherapy.

Fig. 5Cshows that the average cell viability of NCI-N87 cells remained over 95 % after HFB or HFB + laser treatment. This proves that the nanoparticles are safe and biocompatible. In addition, we observed HFB hemolysis activity and demonstrated that it was just as effective as PBS in treating hemolysis (Fig. 5D), indicating that HFB is highly hemocompatible.

3.5. *In vitro studies*

A ROS-sensitive probe called 2′,7′- dichlorodihydrofluorescein diacetate (DCFH-DA) was used to detect the intercellular ROS [50]. Without laser irradiation, the photosensitizer does not generate ROS, and ICG had little effect on the green fluorescent of the DCFH-DA (DCF) when compared with SGC-7901 cells treated with PBS. Fig. 6 shows that cells' fluorescence intensity increased 1.7-fold when PTX@HFB or HFB@IP was present, indicating that PTX might improve intracellular ROS. Specifically, the intracellular ROS was significantly amplified when subjected to laser irradiation (636 nm), most likely due to the $_1O^2$ generated by ICG@HFB. In laser irradiation 636 nm, the best formulation (HFB@IP) was sufficiently potent to provide scope for the PDT effect (Fig. 7A–B).

The CLSM method was used to assess the subcellular localization of HFB@IP in SGC-7901 cells. Dil-labeled PTX intracellular fluorescence overlapped with lysosome green fluorescence and was mainly dispersed in the cytoplasm, as shown in Fig. 7C. As a result of internalization into the acidic and GSH-rich subcellular organelles known as lysosomes, the data show that HFB@IP was able to release its drug.

Fig. 8A confirms, using the AO/EB technique, the nuclear morphology changes and percentages of apoptotic cells associated with apoptosis induction in SGC-7901 cancer cells exposed to ICG, PTX, HFB@IP, and HFB@IP + Laser. This method is known as a qualitative and quantitative approach for identifying apoptosis. Compared to control cells (Fig. 8B), cells treated with IC_{50}
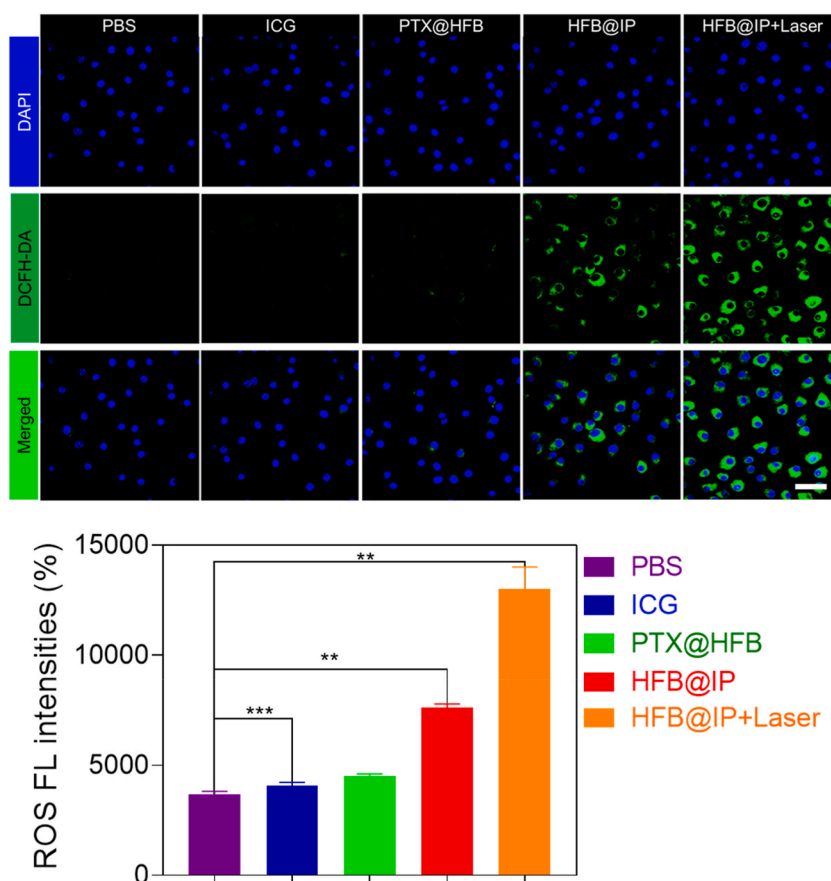

Fig. 6. Intracellular ROS generation of SGC-7901 cells subjected to ICG, PTX@HFB, HFB@IP, and HFB@IP + Laser by DCFH-DA. Scale bar 50 μm. The bar diagram indicates ImageJ analysis of the ROS fluorescence intensities of ICG, PTX@HFB, HFB@IP, and HFB@IP + Laser by DCFH-DA. The data are represented as mean ± standard deviation (SD). (**$P < 0.001$, and ***$P < 0.01$).
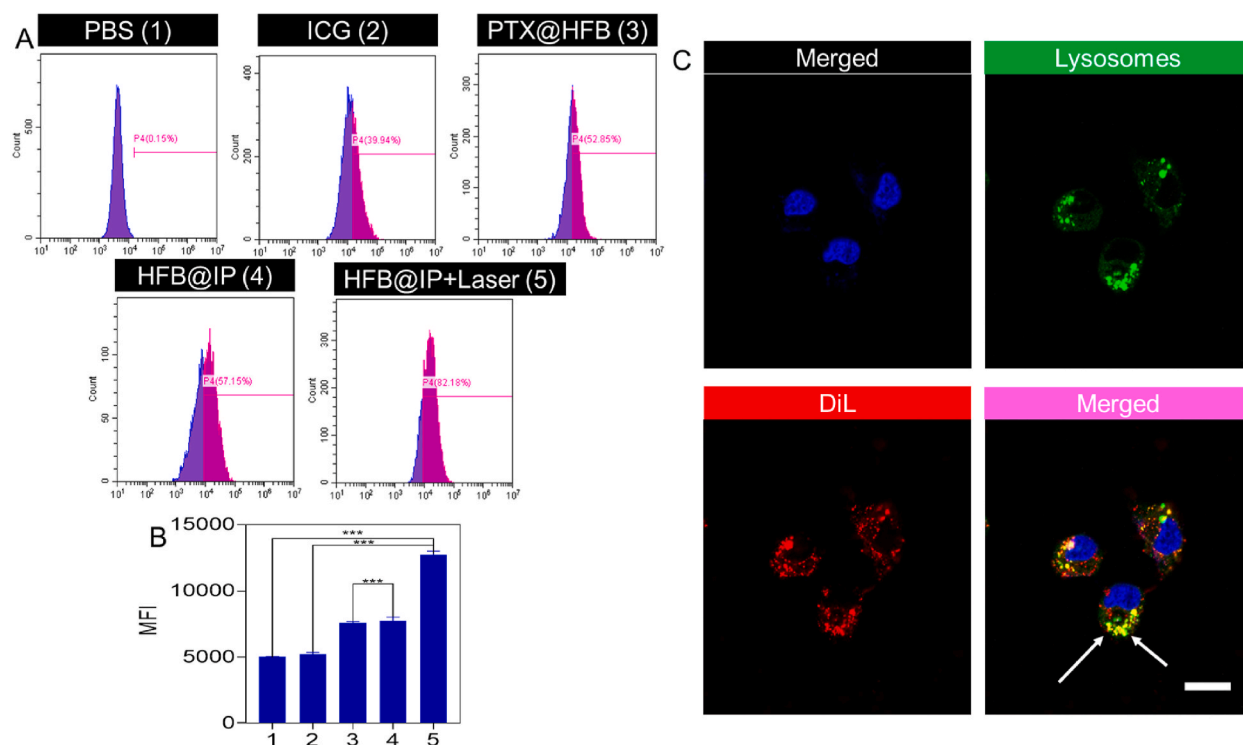
Fig. 7. (A) Flow cytometry investigation of intracellular ROS generation of SGC-7901 cells subjected to ICG, PTX@HFB, HFB@IP, and HFB@IP + Laser by DCFH-DA. (B) The ImageJ analysis of samples' mean fluorescence intensity (MFI). (C) The subcellular localization of HFB@IP in SGC-7901 cells. Scale bar 40 μm. The data are represented as mean ± standard deviation (SD) (***$P < 0.01$).

concentration of ICG, PTX, HFB@IP, and HFB@IP + Laser showed nuclear staining that was green for viable cells and red for apoptotic cells, respectively. In addition, the ratio of apoptotic cells in cells treated with HFB@IP + Laser was significantly higher than in control cells. Furthermore, compared to those treated in ICG and PTX, cells treated with HFB@IP + Laser had more harmful effects on SGC-7901 cells.

Annexin V-FITC/propidium iodide double-staining and flow cytometry were used to further measure cell death in SGC-7901 cells that were treated with IC_{50} concentration of ICG, PTX, HFB@IP, and HFB@IP + Laser. Phosphatidylserine is left on the outer leaflet of the plasma membrane by apoptotic cells when their membrane phospholipid asymmetry is lost [51]. As a result, the presence of phosphatidylserine on the cell membrane can be detected by using Annexin V, a calcium-dependent phospholipid-binding protein with a high affinity for phosphatidylserine, as a marker of apoptosis. The plasma membrane of living cells excludes propidium iodide, a nonspecific DNA intercalating substance. This allows supravital labeling without prior permeabilization to differentiate necrotic cells from apoptotic and living cells. In Fig. 8C, the results are displayed. Dot plots show the representative SGC-7901 and MGC80-3 cell staining with Annexin V/propidium iodide, and Fig. 8D depicts the percentages of apoptotic cells that were determined. A large number of apoptotic cells were detected, however, in the groups that were treated with HFB@IP + Laser. This suggests that the amount of ICG, PTX, HFB@IP, and HFB@IP + Laser induce apoptosis in SGC-7901 cells. These findings further prove that HFB@IP + Laser can trigger cell death in SGC-7901 cells on the path to cell death.

The cytotoxicity of PBS, HFB@IP, ICG + Laser, and HFB@IP + Laser was assessed in the presence of necroptosis inhibitor (necrostatin-1, Nec-1), apoptosis inhibitor (Z-VAD-FMK), and ROS scavenger (N-acetyl-L-cysteine, NAC) to examine further into the mechanism of cell death (Fig. 9). The inhibitors (Nec-1 and Z-VAD-FMK) increased the cell survival of SGC-7901 cells relative to the control group, proving that both pathways contribute to cell death (apoptosis and necroptosis). It is worth mentioning that NAC reduced the cytotoxicity of ICG + Laser and HFB@IP + Laser but had no effect on the anticancer effect of HFB@IP (in the absence of laser irradiation). This indicates that the ICG-based PDT produces reactive oxygen species (ROS) to cause cancer cell death, whereas the cytotoxicity of PTX does not depend on ROS. The findings provide more evidence that the photodynamic and chemotherapy caused cell death and necrosis.

4. Conclusion

To summarise, a drug delivery system that responds to changes in pH and redox milieu has been established by attaching BSA-FA to the surface of HMSNs via pH-sensitive imine linkages. Incorporating BSA-FA significantly enhanced the stability and biocompatibility of nanoparticles while conferring the system with active directing capabilities. Furthermore, the evidence has demonstrated that the
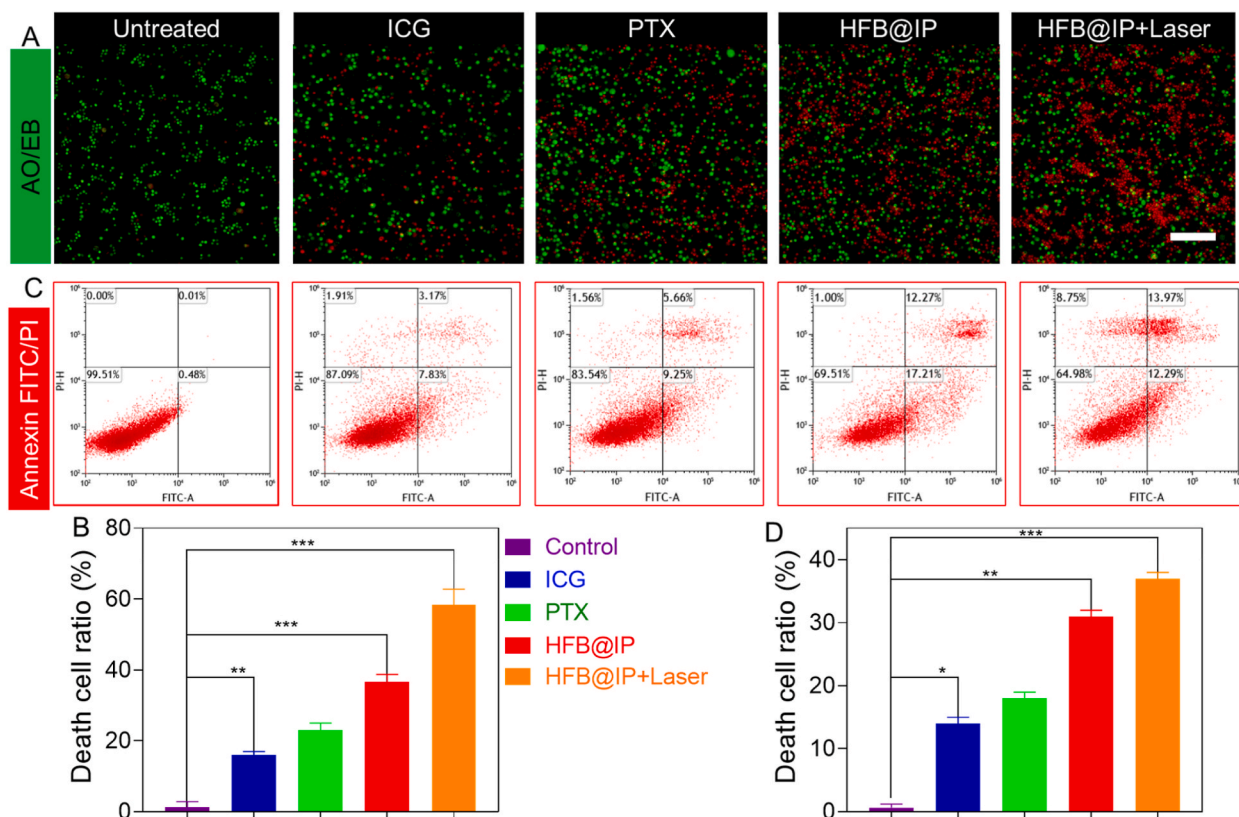
Fig. 8. (A) Dual acridine orange/ethidium bromide (AO/EB) staining of SGC-7901 cells treated with ICG, PTX, HFB@IP, and HFB@IP + Laser (IC$_{50}$ concentration) for 24 h. Scale bar 100 μm. (B) Respective cell death ratio. (C) Investigation of SGC-7901 cells treated with ICG, PTX, HFB@IP, and HFB@IP + Laser (IC$_{50}$ concentration) for 24 h by flow cytometry. (D) Respective cell death ratio. The data are represented as mean ± standard deviation (SD). (*$P < 0.05$, **$P < 0.001$, and ***$P < 0.01$).
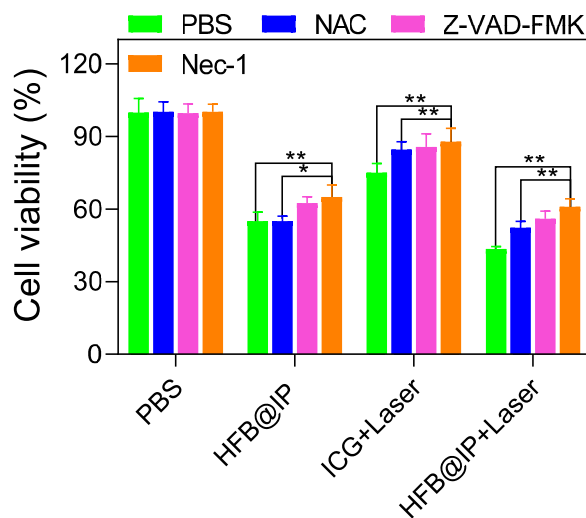

Fig. 9. The cells viability of SGC-7901 cells were incubated with PBS, HFB@IP, ICG + Laser, and HFB@IP + Laser in 1 mM NAC, 20 μM Z-VAD-FMK, and 20 μM Nec-1. The data are represented as mean ± standard deviation (SD). (*$P < 0.05$, **$P < 0.001$, and ***$P < 0.01$).

HFB@IP formulation can efficiently penetrate cancerous cells by endocytosis. The photosensitizer (ICG) and anticancer drug (PTX) were released in a specific area due to high levels of GSH and an acidic milieu. This release led to a substantial increase in cancer cell apoptosis when exposed to laser irradiation. Consequently, the HFB@IP has significant applications and prospective benefits in gastric

cancer treatment.

Ethical approval

Not applicable.

Fundings

Not applicable.

Consent for publication

Not applicable.

Data availability statement

The data that support the findings of this study are available from the corresponding author, upon reasonable request.

CRediT authorship contribution statement

Yuanwei Zhang: Writing – original draft, Software, Methodology, Investigation, Formal analysis, Data curation, Conceptualization. **Yuanxiao Liang:** Writing – review & editing, Supervision, Formal analysis, Conceptualization.

Declaration of competing interest

The authors declare that they have no known competing financial interests or personal relationships that could have appeared to influence the work reported in this paper.

Appendix A. Supplementary data

Supplementary data to this article can be found online at https://doi.org/10.1016/j.heliyon.2024.e29274.

References

[1] H. Sung, J. Ferlay, R.L. Siegel, M. Laversanne, I. Soerjomataram, A. Jemal, F. Bray, Global cancer statistics 2020: GLOBOCAN estimates of incidence and mortality worldwide for 36 cancers in 185 countries, CA A Cancer J. Clin. 71 (2021) 209–249.
[2] T.H. Patel, M. Cecchini, Targeted therapies in advanced gastric cancer, Curr. Treat. Options Oncol. 21 (2020) 1–14.
[3] K. Li, A. Zhang, X. Li, H. Zhang, L. Zhao, Advances in clinical immunotherapy for gastric cancer, Biochim. Biophys. Acta, Rev. Cancer 1876 (2021) 188615.
[4] J. Machlowska, J. Baj, M. Sitarz, R. Maciejewski, R. Sitarz, Gastric cancer: epidemiology, risk factors, classification, genomic characteristics and treatment strategies, Int. J. Mol. Sci. 21 (2020) 4012.
[5] R.E. Sexton, M.N. Al Hallak, M. Diab, A.S. Azmi, Gastric cancer: a comprehensive review of current and future treatment strategies, Cancer Metastasis Rev. 39 (2020) 1179–1203.
[6] N.J. Rakhmatovich, N.D. Fakhriddinovna, Immediate results of surgical treatment of gastric cancer, Int. J. Orange Technol. 3 (2021) 62–65.
[7] S. Catanese, F. Lordick, Targeted and immunotherapy in the era of personalised gastric cancer treatment, Best Pract. Res. Clin. Gastroenterol. 50 (2021) 101738.
[8] S. Lu, C. Zhang, J. Wang, L. Zhao, G. Li, Research progress in nano-drug delivery systems based on the characteristics of the liver cancer microenvironment, Biomed, Pharmacotherapy 170 (2024) 116059.
[9] J. Yan, X. Long, Y. Liang, F. Li, H. Yu, Y. Li, Z. Li, Y. Tian, B. He, Y. Sun, Nanodrug delivery systems and cancer stem cells: from delivery carriers to treatment, Colloids Surf. B Biointerfaces (2022) 112701.
[10] J. Shao, R. Liang, D. Ding, X. Zheng, X. Zhu, S. Hu, H. Wei, B. Wei, A smart multifunctional nanoparticle for enhanced near-infrared image-guided photothermal therapy against gastric cancer, Int. J. Nanomed. (2021) 2897–2915.
[11] X. Guan, K. Zhang, X. Mei, Z. He, S. Su, J. Yang, J. Lv, L. Yuan, X. Duan, W. Guo, Recent progress of nano-drug delivery systems in gastrointestinal cancer, Mater. Express. 13 (2023) 1631–1644.
[12] L. Palanikumar, M. Kalmouni, T. Houhou, O. Abdullah, L. Ali, R. Pasricha, R. Straubinger, S. Thomas, A.J. Afzal, F.N. Barrera, pH-responsive upconversion mesoporous silica nanospheres for combined multimodal diagnostic imaging and targeted photodynamic and photothermal cancer therapy, ACS Nano 17 (2023) 18979–18999.
[13] S. Mohanan, C.I. Sathish, K. Ramadass, M. Liang, A. Vinu, Design and synthesis of cabazitaxel loaded core-shell mesoporous silica nanoparticles with different morphologies for prostate cancer therapy, Small (2023) 2303269.
[14] M. Iranshahy, M.Y. Hanafi-Bojd, S.H. Aghili, M. Iranshahi, S.M. Nabavi, S. Saberi, R. Filosa, I.F. Nezhad, M. Hasanpour, Curcumin-loaded mesoporous silica nanoparticles for drug delivery: synthesis, biological assays and therapeutic potential–a review, RSC Adv. 13 (2023) 22250–22267.
[15] Y. Feng, Z. Liao, M. Li, H. Zhang, T. Li, X. Qin, S. Li, C. Wu, F. You, X. Liao, Mesoporous silica nanoparticles-based nanoplatforms: basic construction, current state, and emerging applications in anticancer therapeutics, Adv. Healthcare Mater. 12 (2023) 2201884.
[16] I. Garrido-Cano, A. Adam-Artigues, A. Lameirinhas, J.F. Blandez, V. Candela-Noguera, A. Lluch, B. Bermejo, F. Sancenón, J.M. Cejalvo, R. Martínez-Máñez, Delivery of miR-200c-3p using tumor-targeted mesoporous silica nanoparticles for breast cancer therapy, ACS Appl. Mater. Interfaces 15 (2023) 38323–38334.
[17] K. Wang, J. Lu, J. Li, Y. Gao, Y. Mao, Q. Zhao, S. Wang, Current trends in smart mesoporous silica-based nanovehicles for photoactivated cancer therapy, J. Contr. Release 339 (2021) 445–472.

[18] F. Ahmadi, A. Sodagar-Taleghani, P. Ebrahimnejad, S.P.H. Moghaddam, F. Ebrahimnejad, K. Asare-Addo, A. Nokhodchi, A review on the latest developments of mesoporous silica nanoparticles as a promising platform for diagnosis and treatment of cancer, Int. J. Pharm. (2022) 122099.

[19] R. Thapa, H. Ali, O. Afzal, A.A. Bhat, W.H. Almalki, S.I. Alzarea, I. Kazmi, A.S.A. Altamimi, N. Jain, M. Pandey, Unlocking the potential of mesoporous silica nanoparticles in breast cancer treatment, J. Nanoparticle Res. 25 (2023) 169.

[20] C. Fan, X. Wang, Y. Wang, Z. Xi, Y. Wang, S. Zhu, M. Wang, L. Xu, Fabricating a PDA-liposome dual-film coated hollow mesoporous silica nanoplatform for chemo-photothermal synergistic antitumor therapy, Pharmaceutics 15 (2023) 1128.

[21] Y.-J. Cheng, J.-J. Hu, S.-Y. Qin, A.-Q. Zhang, X.-Z. Zhang, Recent advances in functional mesoporous silica-based nanoplatforms for combinational photo-chemotherapy of cancer, Biomaterials 232 (2020) 119738.

[22] B. Sun, H. Chen, Y. Wang, X. Wang, W.H.Z. He, C. Xie, F. Lu, Q. Fan, Development of mesoporous silica-based nanoparticles for cancer phototherapy, Dyes Pigments (2023) 111881.

[23] N.B. Fernandes, Y. Nayak, S. Garg, U.Y. Nayak, Multifunctional engineered mesoporous silica/inorganic material hybrid nanoparticles: theranostic perspectives, Coord. Chem. Rev. 478 (2023) 214977.

[24] P. Song, G. Xu, G. Peng, L. Gui, W. Li, W. Li, L. Zhu, Y. Tao, W. Zhang, F. Ge, Nanoporous silica nanoparticles coated with peptide P14 and decorated with 5-fluorouracil and indocyanine green for NIR-triggered photothermal/photodynamic therapy, ACS Appl. Nano Mater. (2023).

[25] H. Meng, M. Xue, T. Xia, Z. Ji, D.Y. Tarn, J.I. Zink, A.E. Nel, Use of size and a copolymer design feature to improve the biodistribution and the enhanced permeability and retention effect of doxorubicin-loaded mesoporous silica nanoparticles in a murine xenograft tumor model, ACS Nano 5 (2011) 4131–4144.

[26] Y. Wang, J. Zhang, X. Lv, L. Wang, Z. Zhong, D.-P. Yang, W. Si, T. Zhang, X. Dong, Mitoxantrone as photothermal agents for ultrasound/fluorescence imaging-guided chemo-phototherapy enhanced by intratumoral H_2O_2-Induced CO, Biomaterials 252 (2020) 120111, https://doi.org/10.1016/j.biomaterials.2020.120111.

[27] H. Jin, T. Zhu, X. Huang, M. Sun, H. Li, X. Zhu, M. Liu, Y. Xie, W. Huang, D. Yan, ROS-responsive nanoparticles based on amphiphilic hyperbranched polyphosphoester for drug delivery: light-triggered size-reducing and enhanced tumor penetration, Biomaterials 211 (2019) 68–80, https://doi.org/10.1016/j.biomaterials.2019.04.029.

[28] M. Habibi Jouybari, S. Hosseini, K. Mahboobnia, L.A. Boloursaz, M. Moradi, M. Irani, Simultaneous controlled release of 5-FU, DOX and PTX from chitosan/PLA/5-FU/g-C3N4-DOX/g-C3N4-PTX triaxial nanofibers for breast cancer treatment in vitro, Colloids Surf. B Biointerfaces 179 (2019) 495–504, https://doi.org/10.1016/j.colsurfb.2019.04.026.

[29] J. Wen, Y. Lv, Y. Xu, P. Zhang, H. Li, X. Chen, X. Li, L. Zhang, F. Liu, W. Zeng, S. Sun, Construction of a biodegradable, versatile nanocarrier for optional combination cancer therapy, Acta Biomater. 83 (2019) 359–371, https://doi.org/10.1016/j.actbio.2018.11.009.

[30] H. Maleki, M.R. Hosseini Najafabadi, T.J. Webster, M.R. Hadjighassem, E. Sadroddiny, H. Ghanbari, M. Khosravani, M. Adabi, Effect of Paclitaxel/etoposide co-loaded polymeric nanoparticles on tumor size and survival rate in a rat model of glioblastoma, Int. J. Pharm. 604 (2021) 120722, https://doi.org/10.1016/j.ijpharm.2021.120722.

[31] F. Badparvar, A.P. Marjani, R. Salehi, F. Ramezani, pH/redox responsive size-switchable intelligent nanovehicle for tumor microenvironment targeted DOX release, Sci. Rep. 13 (2023) 22475.

[32] S. Yadav, K. Ramesh, O.S. Reddy, V. Karthika, P. Kumar, S.-H. Jo, S.I.I. Yoo, S.-H. Park, K.T. Lim, Redox-responsive comparison of diselenide and disulfide core-cross-linked micelles for drug delivery application, Pharmaceutics 15 (2023) 1159.

[33] Z. Li, Y. Ma, Y. Ren, X. Lin, Z. Su, S. Zhang, Thermal-triggered loading and GSH-responsive releasing property of HBc particles for drug delivery, J. Contr. Release (2023).

[34] X. Mu, C. Yan, Q. Tian, J. Lin, S. Yang, BSA-assisted synthesis of ultrasmall gallic acid-Fe(III) coordination polymer nanoparticles for cancer theranostics, Int. J. Nanomed. 12 (2017) 7207–7223, https://doi.org/10.2147/IJN.S146064.

[35] R. Liu, C. Hu, Y. Yang, J. Zhang, H. Gao, Theranostic nanoparticles with tumor-specific enzyme-triggered size reduction and drug release to perform photothermal therapy for breast cancer treatment, Acta Pharm. Sin. B 9 (2019) 410–420, https://doi.org/10.1016/j.apsb.2018.09.001.

[36] X. Zhang, R. Zhang, J. Huang, M. Luo, X. Chen, Y. Kang, J. Wu, Albumin enhances PTX delivery ability of dextran NPs and therapeutic efficacy of PTX for colorectal cancer, J. Mater. Chem. B 7 (2019) 3537–3545, https://doi.org/10.1039/C9TB00181F.

[37] A.B. Madhankumar, O.D. Mrowczynski, S.R. Patel, C.L. Weston, B.E. Zacharia, M.J. Glantz, C.A. Siedlecki, L.-C. Xu, J.R. Connor, Interleukin-13 conjugated quantum dots for identification of glioma initiating cells and their extracellular vesicles, Acta Biomater. 58 (2017) 205–213, https://doi.org/10.1016/j.actbio.2017.06.002.

[38] K. Zhou, Y. Zhu, X. Chen, L. Li, W. Xu, Redox- and MMP-2-sensitive drug delivery nanoparticles based on gelatin and albumin for tumor targeted delivery of paclitaxel, Mater. Sci. Eng., C 114 (2020) 111006, https://doi.org/10.1016/j.msec.2020.111006.

[39] M.F. Sanad, E.S. Abu Serea, S.M. Bazid, S. Nabih, M.A. Ahsan, A.E. Shalan, High cytotoxic activity of ZnO@leucovorin nanocomposite based materials against an MCF-7 cell model, Anal. Methods 12 (2020) 2176–2184, https://doi.org/10.1039/D0AY00498G.

[40] M.T. de Melo, H.L. Piva, A.C. Tedesco, Design of new protein drug delivery system (PDDS) with photoactive compounds as a potential application in the treatment of glioblastoma brain cancer, Mater. Sci. Eng., C 110 (2020) 110638, https://doi.org/10.1016/j.msec.2020.110638.

[41] R. Zhao, G. Zheng, L. Fan, Z. Shen, K. Jiang, Y. Guo, J.-W. Shao, Carrier-free nanodrug by co-assembly of chemotherapeutic agent and photosensitiser for cancer imaging and chemo-photo combination therapy, Acta Biomater. 70 (2018) 197–210, https://doi.org/10.1016/j.actbio.2018.01.028.

[42] Y. Li, X. Zhi, J. Lin, X. You, J. Yuan, Preparation and characterisation of DOX loaded keratin nanoparticles for pH/GSH dual responsive release, Mater. Sci. Eng., C 73 (2017) 189–197, https://doi.org/10.1016/j.msec.2016.12.067.

[43] X. Li, X. Zhao, D. Pardhi, Q. Wu, Y. Zheng, H. Zhu, G. Mao, Folic acid modified cell membrane capsules encapsulating doxorubicin and indocyanine green for highly effective combinational therapy in vivo, Acta Biomater. 74 (2018) 374–384, https://doi.org/10.1016/j.actbio.2018.05.006.

[44] V. Hosseini, M. Mirrahimi, A. Shakeri-Zadeh, F. Koosha, B. Ghalandari, S. Maleki, A. Komeili, S.K. Kamrava, Multimodal cancer cell therapy using Au@Fe2O3 core–shell nanoparticles in combination with photo-thermo-radiotherapy, Photodiagnosis Photodyn. Ther. 24 (2018) 129–135, https://doi.org/10.1016/j.pdpdt.2018.08.003.

[45] D. Fischer, Y. Li, B. Ahlemeyer, J. Krieglstein, T. Kissel, In vitro cytotoxicity testing of polycations: influence of polymer structure on cell viability and hemolysis, Biomaterials 24 (2003) 1121–1131, https://doi.org/10.1016/S0142-9612(02)00445-3.

[46] Y. Hu, D. Yu, X. Zhang, 9-amino acid cyclic peptide-decorated sorafenib polymeric nanoparticles for the efficient in vitro nursing care analysis of hepatocellular carcinoma, Process Biochem. 100 (2021) 140–148, https://doi.org/10.1016/j.procbio.2020.09.021.

[47] X. Li, Y. Gao, Synergistically fabricated polymeric nanoparticles featuring dual drug delivery system to enhance the nursing care of cervical cancer, Process Biochem. 98 (2020) 254–261, https://doi.org/10.1016/j.procbio.2020.09.010.

[48] J.-J. Hu, M.-D. Liu, Y. Chen, F. Gao, S.-Y. Peng, B.-R. Xie, C.-X. Li, X. Zeng, X.-Z. Zhang, Immobilised liquid metal nanoparticles with improved stability and photothermal performance for combinational therapy of tumor, Biomaterials 207 (2019) 76–88, https://doi.org/10.1016/j.biomaterials.2019.03.043.

[49] H. Zhu, J. Tao, W. Wang, Y. Zhou, P. Li, Z. Li, K. Yan, S. Wu, K.W.K. Yeung, Z. Xu, H. Xu, P.K. Chu, Magnetic, fluorescent, and thermo-responsive Fe3O4/rare earth incorporated poly(St-NIPAM) core–shell colloidal nanoparticles in multimodal optical/magnetic resonance imaging probes, Biomaterials 34 (2013) 2296–2306, https://doi.org/10.1016/j.biomaterials.2012.11.056.

[50] V. Ramalingam, S. Revathidevi, T.S. Shanmuganayagam, L. Muthulakshmi, R. Rajaram, Gold nanoparticle induces mitochondria-mediated apoptosis and cell cycle arrest in nonsmall cell lung cancer cells, Gold Bull. 50 (2017) 177–189, https://doi.org/10.1007/s13404-017-0208-x.

[51] G. Koopman, C.P. Reutelingsperger, G.A. Kuijten, R.M. Keehnen, S.T. Pals, M.H. Van Oers, Annexin V for Flow Cytometric Detection of Phosphatidylserine Expression on B Cells Undergoing Apoptosis, 1994.